The Journal of Experimental Biology 210, 2676-2690
Published by The Company of Biologists 2007
doi:10.1242/jeb.004580

Skeletal strain patterns and growth in the emu hindlimb during ontogeny

Russell P. Main* and Andrew A. Biewener

Concord Field Station, Department of Organismic and Evolutionary Biology, Harvard University, 100 Old Causeway Road, Bedford, MA 01730, USA

*Author for correspondence at present address: Sibley School of Mechanical and Aerospace Engineering, 187 Grumman Hall, Cornell University, Ithaca, NY 14853, USA (e-mail: rpm74@cornell.edu)

Accepted 27 March 2007

Summary

Most studies examining changes in mechanical performance in animals across size have typically focused on inter-specific comparisons across large size ranges. Scale effects, however, can also have important consequences in vertebrates as they increase in size and mass during ontogeny. The goal of this study was to examine how growth and development in the emu (*Dromaius novaehollandiae*) hindlimb skeleton reflects the demands placed upon it by ontogenetic changes in locomotor mechanics and body mass. Bone strain patterns in the femur and tibiotarsus (TBT) were related to ontogenetic changes in limb kinematics, ground reaction forces, and ontogenetic scaling patterns of the cross-sectional bone geometry, curvature and mineral ash content over a 4.4-fold increase in leg length and 65-fold increase in mass. Although the distribution of principal and axial strains remained similar in both bones over the ontogenetic size range examined, principal strains on the cranial femur and caudal femur and TBT increased significantly during growth. The ontogenetic increase in principal strains in these bones was likely caused by isometry or only slight positive allometry in bone cross-sectional geometry during growth, while relative limb loading remained similar. The growth-related increase in bone strain magnitude was likely mitigated by increased bone mineralization and decreased curvature. Throughout most of ontogeny, shear strains dominated loading in both bones. This was reflected in the nearly circular cross-sectional geometry of the femur and TBT, suggesting selection for resistance to high torsional loads, as opposed to the more eccentric cross-sectional geometries often associated with the bending common to tetrapods with parasagittal limb orientations, for which *in vivo* bone strains have typically been measured to date.

Key words: bone, scaling, ontogeny, growth, bone strain, bone geometry, torsion, emu.

Introduction

Scaling, or the relative change in organismal dimensions, affects many aspects of vertebrate biology. Whether concerning metabolic rates (Taylor et al., 1970; Full and Tu, 1991; Schmidt-Nielsen, 1997), prey capture and food processing mechanisms (Richard and Wainwright, 1995; Herring et al., 2005; Herrel and O'Reilly, 2006), muscle–tendon mechanics (Biewener, 1989; Biewener, 2005; Pollock and Shadwick, 1994), or skeletal support during locomotion (Alexander et al., 1979a; Biewener, 1982; Biewener, 1983; Olmos et al., 1996; Cubo and Casinos, 1998), differences in physiological and biomechanical performance that result from changes in body size are critical to an organism's success.

Although most studies have examined scale effects across an inter-specific size range, changes in size during ontogenetic growth can have important implications for performance in growing animals as well. Specifically, ontogenetic scaling of the musculoskeletal anatomy of the limbs has important consequences for locomotor mechanics and life history strategies. Two studies showed how musculoskeletal allometry and changing material properties of the limb bones through growth can affect locomotor performance at different ontogenetic stages (Carrier, 1983; Carrier and Leon, 1990). In the California gull *Larus californicus* (Carrier and Leon, 1990), ontogenetic scaling of the musculoskeletal system and increased elastic moduli in the bones of fledgling birds demonstrated the coordinated development of the anatomy required for powered flight with the achievement of adult wing bone length and mineralization. In the highly precocial jack rabbit *Lepus californicus*, Carrier described another ontogenetic strategy, in which metatarsal length scaled with positive allometry, while muscle mass and mechanical advantage of the gastrocnemius at the ankle and the second moment of area of the metatarsals (a measure of their bending resistance) scaled with negative allometry (Carrier, 1983). From these scaling patterns, Carrier concluded that, for their mass, younger rabbits could generate relatively larger propulsive forces at the ankle without an increased fracture risk of the metatarsals, which were composed of relatively weaker bone tissue than in adult rabbits. These concerted scaling patterns allowed the musculoskeletal system of the young hares to be capable of producing large enough forces to achieve adult escape velocities early in ontogenetic growth. Similar ontogenetic

scaling relationships were observed between the triceps brachii moment arm and forelimb length in capuchin monkeys *Cebus* spp. (Young, 2005).

In addition to examining changes in musculoskeletal morphology and performance, *in vivo* mechanical measurements can provide further important insight into the development of the musculoskeletal system and ontogenetic changes in locomotor performance. Based upon measurements of limb loading and *in vivo* bone strains, ontogenetic scaling patterns in the goat radius were hypothesized to be partly responsible for allowing young goats to perform safely at similar absolute speeds as adult goats (Main and Biewener, 2004). When traveling at the same speeds as adults, the less well-mineralized radii of juvenile goats experienced much lower strains than the radii of adult goats, which were moving at lower relative speeds. Strong negative growth allometry in the cross-sectional area (A) and second moments of area (I) meant that the young goats had more robust radii for their size, giving them safety factors likely 3–6 times higher than adult goats during galloping (Main and Biewener, 2006). In contrast, bone strain magnitudes in the chicken tibiotarsus (TBT) were generally maintained at similar levels during ontogenetic growth (Biewener et al., 1986) despite A and I scaling with negative allometry and isometry, respectively (Biewener and Bertram, 1994). As in the chicken femur, the TBT also experienced a significant torsional component (Biewener et al., 1986; Biewener and Bertram, 1994; Carrano and Biewener, 1999), though the polar moment of area (J, indicating a bone's resistance to torsion) also scaled isometrically through ontogeny. Because the cross-sectional geometry of the chicken TBT did not scale with the strong positive allometry required to maintain similar strains, other locomotor or skeletal parameters such as limb kinematics, posture, limb loading, bone curvature or bone mineralization must have changed during growth to help reduce bone strains in older, larger individuals of this species. However, ontogenetic scaling patterns of these variables were not reported.

The goal of the present study was to use an integrative approach to address how growth and development in the limb skeleton reflect the demands placed upon it by ontogenetic changes in locomotor mechanics and body mass. We addressed this goal by collecting *in vivo* bone strain data from the emu femur and TBT over a 65-fold ontogenetic increase in body mass, while also accounting for ontogenetic changes in limb loading, kinematics, bone curvature, and bone mineral content, in addition to the measures of cross-sectional bone geometry, with the following predictions. (1) Similar to previous studies of ontogenetic skeletal mechanics (Biewener et al., 1986; Main and Biewener, 2004), the distribution of mid-shaft bone strains in the emu femur and TBT would remain consistent during ontogeny, and like the chicken TBT, also remain similar in magnitude. (2) Given nearly isometric growth in bone cross-sectional geometry, as was observed for the chicken TBT (Biewener and Bertram, 1994), the maintenance of strain magnitudes in the emu femur and TBT through ontogeny would be accomplished by some combination of the following: (i) an increase in bone mineralization, (ii) a decrease in longitudinal bone curvature, (iii) a decrease in relative limb loading, or (iv) a more 'upright' posture in larger emu. (3) Similar to the chicken femur and TBT, we expected the strain environment in the emu femur and TBT to be dominated by torsional loading, with relatively smaller contributions from axial bending and compressive strains.

Materials and methods

Animals

Emu (*Dromaius novaehollandiae*) Mathews were obtained from commercial farms (Songline Emu Farm, Gill, MA, USA; N=20; Scattered Oaks Emu Farm, Iola, TX, USA; N=6; Deep Hollow Farm, Oakdale, CT, USA; N=4) as hatchlings and raised at Harvard University's Concord Field Station in indoor enclosures up to 8 weeks of age and in large outdoor paddocks thereafter. The birds had free access to commercial ratite diet (Mazuri, PMI Nutrition International, LLC, Brentwood, MO, USA) and water. Thirty birds were included in various parts of the study, ranging in mass and age from 2 week-old, 0.74 kg hatchlings to >8 year-old, 51.7 kg adults, with sexual maturity occurring at about 80 weeks (Davies, 2002). Over the growth period examined, total hindlimb length increased 4.4-fold from 0.27 m to 1.20 m.

Ground reaction force recordings

Ground reaction force (GRF) data were collected from 25 birds over the size range examined to measure changes in relative limb loading during ontogeny. GRFs were also recorded before and after surgery to implant strain gauges on the femur and tibiotarsus (TBT) to assess whether any post-surgical lameness in the limb occurred. Before GRF data were collected, both hindlimbs were plucked or shaved, and the following centers of joint rotation and anatomical landmarks identified and marked with non-toxic white paint: a point on the caudal-most border of the ischium, the hip, knee, ankle, tarsometatarsal-phalangeal joint (TMP), and the distal phalanx on the middle toe (Fig. 1). Segment lengths were measured as the distance between these points.

The GRF data were recorded using one or two (in series) Kistler force plates (0.4 m×0.6 m; 9286A, Kistler, Amherst, NY, USA) and an A/D converter (Bioware 3.2, Kistler) sampling at 2.5 kHz. The birds were simultaneously filmed from a lateral view (Redlake Motionscope PCI, San Diego, CA, USA) at 250 Hz, to record which limbs made contact with the force plates and the timing of each foot contact. A trigger pulse, to start the camera, was also recorded by the A/D converter to synchronize the video and force data. Following data collection, the force data were filtered using a fourth order zero-lag Butterworth filter with a cut-off frequency of 75 Hz to attenuate any artificial noise in the signal. Following this, a custom MATLAB program (The Mathworks, Inc., Natick, MA, USA) calculated the peak resultant GRF ($\mathbf{F}_R$) for each footfall and the orientation of the force vector relative to the vertical reference frame. Peak $\mathbf{F}_R$ was normalized by the bird's body weight BW ($\mathbf{F}_R$/BW) to assess ontogenetic patterns in limb loading. By digitizing the position of the ischium marker through time and recording the timing of foot-down and foot-off for each trial, the relationship between each bird's average forward speed (m s^{-1}) and duty factor (the fraction of the stride period that a bird's foot was in contact with the ground) was determined and used to obtain target speeds for the post-operative treadmill strain recordings.

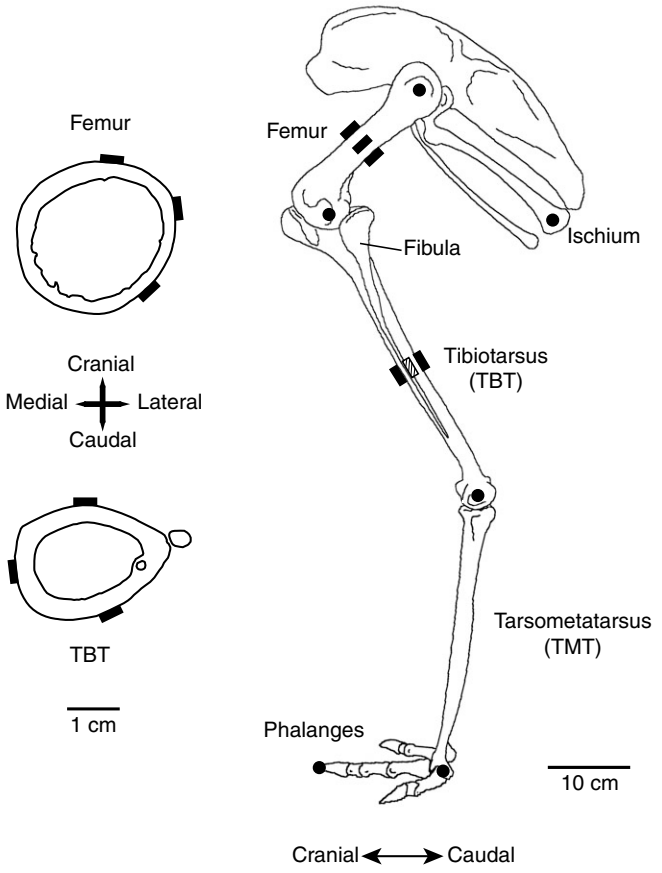

Fig. 1. A lateral view of the left hindlimb skeleton and pelvis of an adult emu with representative mid-shaft cross-sections for the femur and tibiotarsus (TBT). The gauge positions in the cross-sections and at the femur and TBT mid-shafts are indicated with black rectangles. On the hindlimb skeleton, the gauge position for the medial TBT is indicated by a hatched rectangle on the lateral surface. The kinematic markers analyzed are indicated with black circles and are as follows: the ischium, hip, knee, ankle, tarsometatarsal-phalangeal joint (TMP), and the distal end of the middle toe.

Surgical procedures

The day following pre-operative GRF recordings, aseptic surgery was conducted to attach strain gauges to each bird's left femur and TBT. Depending on the size of the animal, the birds were induced for surgery either through mask inhalation of isoflurane (2–3%) or with a mixed intramuscular injection of xylazine (3–3.5 mg kg^{-1}) and ketamine (15–17.5 mg kg^{-1}) to the right lateral gastrocnemius. After induction, the birds were maintained at a surgical anesthetic plane through mask inhalation of isoflurane (1–4%). Breathing and heart rate were monitored throughout surgery, and the anesthesia adjusted as necessary.

To attach strain gauges to the mid-shafts of the femur and TBT, incisions were first made over the lateral surface of the femur and over the synsacrum, just dorsal to the hip, and the strain gauges and their lead wires (36-gauge, etched Teflon^{TM} insulation; Micromeasurements, Raleigh, NC, USA) passed subcutaneously to the bone site. To access the gauge attachment sites at the mid-shaft of the femur, cuts were made with surgical scissors through both the iliotibialis lateralis and femorotibialis externus p. proximalis muscles, directly overlying or originating on the femur (Patak and Baldwin, 1998); making sure to remain parallel to each muscle's fibers. A small portion of the proximal origin of the femorotibialis externus p. distalis muscle was also reflected from the mid-shaft of the femur to allow attachment of a strain gauge to the bone's caudal surface. Once the cranial, caudal and lateral surfaces of the femur were exposed, a small 1–2 cm^2 (depending on the size of the bird) region of the periosteum was removed on each surface, and the underlying mineralized surface lightly scraped with a periosteal elevator. The bone surfaces were defatted and dried using methyl ethyl ketone (Sigma Chemical Co., St Louis, MO, USA). Strain gauges were then bonded to each bone site using a self-catalyzing cyanoacrylate adhesive (Duro, Henkel Loctite Corp., Rocky Hill, CT, USA). After the strain gauges were bonded to the femur, the overlying musculature and skin were sutured (2-0 or 3-0 coated vicryl, Ethicon Inc., Somerville, NJ, USA).

Sterilized rectangular rosette strain gauges of increasing size during growth (FRA-1-11 or FRA-2-11; Tokyo Sokki Kenkyujo Co., Ltd, Tokyo, Japan) were attached to the cranial and caudal surfaces of the femur, while a single element strain gauge (of increasing size: FLK-1-11, FLA-1-11 or FLA-3-11) was attached to the lateral bone surface. Rosette strain gauges allow the tensile and compressive principal strains and their angles (ϕ) relative to the bone's longitudinal axis to be determined, while single element gauges only measure strains along a single axis. The rosette gauges were attached to the cranial and caudal femur surfaces such that the central of the three gauge elements was aligned parallel to the bone's longitudinal axis. The actual angular orientations of the strain gauges were measured *post-mortem* using digital pictures of the gauges on the bones and a clear protractor. The average alignment of the three gauges on the femur was within ±5° (±4°, mean ± s.d. for the three gauges; range: 0–23°) of the bone's longitudinal axis, with the gauges proximal–distal position at the mid-shaft varying by less than 3±2% of the bone's length. Although referred to as 'caudal', the caudal rosette gauge was typically placed in a more caudal-lateral position on the femur (Fig. 1).

To access the cranial, caudal and medial mid-shaft surfaces of the left TBT, an incision was made over the medial mid-shaft of the bone. After exposing the gauge attachment sites by retracting the overlying muscles and mobilizing a small central portion of the flexor digitorum longus muscle, to access the TBT's caudal surface, strain gauges were led subcutaneously from the hip, and the bone surfaces prepared for gauge attachment as for the femur. Single element strain gauges (FLK-1-11, FLA-1-11 or FLA-3-11) were attached to both the cranial and medial mid-shaft surfaces of the TBT, while a rosette gauge (FRA-1-11 or FRA-2-11) was attached to the caudal surface. In two large, nearly adult birds (age: 75 weeks; mass: 38.4 kg and 43.9 kg), rosette gauges (FRA-2-11) were bonded to all three TBT surfaces to measure the orientation of the principal strains on the cranial and medial bone surfaces as well as the caudal surface. The average orientations of the three gauges on the TBT were within ±3° (±2°, range: 0–12°) of the bone's longitudinal axis, with the gauges proximal–distal position at the mid-shaft varying by less than 3±2% of the bone's length.

After the strain gauges were bonded to the three TBT surfaces

and the medial incision sutured, the incision over the synsacrum was closed and the lead wires and pre-soldered epoxy-mounted connector anchored to the skin using 2-0 coated vicryl suture to provide additional strain relief. The connector and incision were then covered with gauze and elastic bandaging tape. Following surgery, each bird was given intramuscular injections of analgesic (flunixin, 1 mg kg^{-1}) and antibiotic (ampicillin, 8 mg kg^{-1}).

Strain data collection

The day following surgery, *in vivo* bone strain data were collected as the birds (N=24) ran on a motorized treadmill over a range of speeds and gaits. While on the treadmill, the lead wire connector over the hip was connected to a 5.5 m shielded cable (NMUF6/30-40465J; Cooner Wire, Chatsworth, CA, USA) secured to the rump of the bird with elastic bandaging tape. The cable was connected to a bridge amplifier (Vishay 2120; Micromeasurements), from which the raw strain signals were sampled by an A/D converter (Axon Instruments, Union City, CA, USA) at 2.0 kHz. During strain data collection, each emu's joint centers were again marked, and lateral-view video data collected at 125 Hz and synchronized to the strain data using a trigger pulse to relate the bone strain recordings to the timing of foot contact, stride length and frequency, two-dimensional joint kinematics and duty factor (DF).

Terrestrial birds do not have distinct gaits that are easily defined by characteristic footfall patterns or the presence/absence of an aerial phase (Gatesy and Biewener, 1991). Thus, gait distinctions in the emu, both during GRF and strain data collection, were made using qualitative assessments of the center of mass movements. From the observed center of mass movements, we estimated that the emu switched from a walk to a run [or grounded run (Rubenson et al., 2004)] at a DF of about 0.60–0.55. This is consistent with previous walk–run transition DFs reported for ostriches and rheas [0.62–0.56 (Gatesy and Biewener, 1991; Rubenson et al., 2004)]. Using the pre-operative over-ground relationships between speed and DF, strain data were collected at speeds corresponding to the following range of DFs: 0.70, 0.65, 0.60, 0.50, 0.45, 0.40 and 0.35, comprising both walking and running gaits. Duty factor was used to define dynamically similar gaits and locomotion between the different sized animals (Alexander and Jayes, 1983), given that animals of different size, moving with the same DF, will support their body weight and movement over the same relative fraction of their stride time.

Given the similarity in ontogenetic strain patterns and principal strain orientations at each speed, only data from birds running with a DF of 0.40 (±0.01), showing a distinct aerial phase, will be presented here, as this speed provided the most repeatable behaviour from the birds. Strain magnitudes did, however, change across speed, with strains at a walk of 0.65DF being about 67% of those when running at a 0.40DF. After both post-surgical bone strain and GRF data collection were completed, each bird was sedated as for surgery and euthanized by an injection of sodium pentobarbital [intramuscular: 600 mg kg^{-1} up to 8 kg body mass (M_b), and intra-cardiac: 300 mg kg^{-1} beyond 8 kg M_b]. All surgical and experimental procedures were approved by the Institutional Animal Care and Use Committee at Harvard University (protocol number 21-08).

Strain data analysis

Raw strain data were filtered using a fourth order zero-lag Butterworth filter with a cut-off frequency of 175 Hz. Data from five consecutive foot contacts were chosen for further analysis, from 1–2 treadmill trials for each bird at each DF. The magnitudes and timing of peak strains for the two trials were highly repeatable for each bird, producing mean coefficients of variation of 0.07 and 0.06, respectively.

The raw strain data were analyzed using a custom MATLAB program that zeroed and calibrated the strain recordings, converting voltages to microstrain ($\mu\varepsilon$, strain$\times10^{-6}$) based on a 1000 $\mu\varepsilon$ shunt calibration of the Vishay amplifier. Zero strain levels were determined during the swing phase of the limb, when the voltage change in the strain signal was minimal. Raw strain data from the rosette strain gauges were converted to principal strains (tension and compression) and the orientation of these strains (ϕ) determined using standard equations that assume a uniaxial planar state of strain (Biewener, 1992). Principal strains and strains recorded by the single element gauges were adjusted for any post-surgical lameness in the limb ($\mu\varepsilon\times\mathbf{F}_R$ pre-surgery/$\mathbf{F}_R$ post-surgery), assuming that changes in strain were proportional to changes in limb loading. Post-operative differences in peak $\mathbf{F}_R$ were minimal, averaging slightly higher (104±12%) than pre-surgery peak ground reaction forces.

Peak tensile and compressive principal strains and their orientations, as well as the peak tensile and compressive axial strains measured from the single element gauges, and the percentage of the stance phase when they occurred, were determined for each locomotor cycle. Because strain gauges could not be placed at all four anatomical positions around each bone (cranial, caudal, medial, lateral), peak axial and bending strains measured in both the cranial–caudal (CC) and medial–lateral (ML) directions were calculated by determining the planar distribution of axial strains at the bone's mid-shaft. This was done by mapping the strain recordings from the single element gauges and the central elements of the rosette gauges (after correcting for any gauge misalignment) on to a drawing of each bone's mid-shaft cross-section (see methods below) using a custom MATLAB program (for details, see Biewener, 1992). Once the time-varying patterns of axial strain were determined for each of the four anatomical positions, the axial and bending strains across both anatomical axes (CC and ML) were calculated using equations presented previously (Main and Biewener, 2006). Shear strains were also calculated from data provided by the rosette strain gauges for the cranial and caudal femur and the caudal TBT using standard equations (Biewener and Dial, 1995).

Bone geometry and percent mineral content

After the birds were euthanized, the left femora and TBTs were removed from the limbs and cleaned of muscle and connective tissue. The bones were left to dry for at least 4 weeks at room temperature. Both the CC and ML longitudinal bone curvatures were measured by dividing the radius of curvature for each direction by half the CC or ML diameter of each bone, respectively. The radius of curvature was measured as the orthogonal distance from the CC or ML mid-point of the bone at its mid-shaft, to a line bisecting the proximal and distal ends of each bone (Bertram and Biewener, 1992).

After measuring the radius of curvature, the alignment of the strain gauges, and their placement relative to each bone's mid-shaft, the central third of the instrumented left femora and TBTs (with the fibulae still associated) were embedded in fiberglass resin (Bondo-Mar-Hyde Corp., Atlanta, GA, USA). A 100 μm thin section was taken at the mid-shaft of each bone using a diamond-bladed annular saw (Microslice II; Cambridge Instruments, Ltd, Cambridge, UK). The sections were affixed to microscope slides such that the ML and CC axes were oriented near *x* and *y* reference axes, respectively (as in Fig. 1). A digital picture of each cross-section was taken using a digital camera (Olympus C-5050, Olympus America, Inc., Melville, NY, USA) attached directly to a computer. Each bone cross-section (N=29 and N=30 for the femur and TBT, respectively) was then outlined in Photoshop (v.9.0, Adobe Systems, Inc., San Jose, CA, USA), and from these images the cross-sectional area (A), second moments of area (I_{xx} and I_{yy}), and polar moment of area (J) calculated for each using a custom macro (courtesy of D. Lieberman) for NIH Image 1.61 (Bethesda, MD, USA). The macro determined the axes about which the minimum and maximum second moments of area were distributed. These second moments of area were designated as either I_{xx} or I_{yy}, depending upon which reference axis (x or y) the second moment of area axis lay closer to. Because the minimum and maximum second moments of area were not exactly distributed about the reference axes, the axes determining I_{xx} and I_{yy} did not necessarily correspond to the ML or CC axes, respectively.

For each bird (N=30), a single bone segment, one-tenth the length of each bone, was taken proximal and distal to the central third of each femur and TBT, respectively, to determine the percent mineral content by mass. The periosteum was removed from all bone segments. The marrow and adjacent fibula were removed from each TBT segment, but the trabeculae present in many of the femoral segments were left intact. The bone segments were rinsed in warm water and allowed to dry at room temperature for a day before being placed in an oven to dry for 24 h at 90°C. Following this, each bone segment was weighed (Sartorius 1800, Goettingen, Germany), placed in a small aluminum dish (also separately weighed), and weighed together. The bone segments and the aluminum dishes were then placed in one of two muffle furnaces (Huppert Model 2 Deluxe; Chicago, IL, USA and Lab-Heat; Blue M Electric Co., Blue Island, IL, USA), three at a time, for 12 h at 400°C. Immediately upon removal from the oven, the ashed bone and aluminum dish were weighed again. The percent mineral content by mass of each segment was determined as post-ashed mass/pre-ashed mass×100.

Statistical analyses

For the strain-related data presented in the figures, each data point represents the mean of one or two treadmill trials for each bird, each consisting of five stance periods, while each data point presented for the GRF data represents the mean for a variable number of running trials (range: 1–10), each consisting of one footfall. Although *in vivo* bone strain data were collected from 24 birds, data were not obtained from all six bone sites in every bird because of inoperative gauges. Thus, sample sizes for the strain data were typically less than 24 and varied from 11 to 19 between gauge locations. Error bars are generally omitted for clarity and consistency (three birds are only represented by a single trial for both the GRF data and strain data at 0.40DF), and because the variation between trials was generally small for each bird. For all morphological and the percent ash data, each data point represents a single measurement from each bird. Least-squares regressions (Kaleidagraph 3.6, Synergy Software, Reading, PA, USA) were used to examine ontogenetic patterns for the limb kinematics, bone strains, cross-sectional geometry, bone curvature, and percent mineral content *versus* body mass. All morphological and strain data were fit with a power curve and plotted on logarithmic axes. Log-transformation of data is common practice in scaling studies where power relationships are expected, as it makes the slopes of exponential relationships linear, and thus, more directly comparable between different measures. Significant differences in slope were based upon 95% confidence intervals (CI) derived from the equations and presented as ±95%CI. Where trends were found not to differ significantly from zero, an overall mean (±s.d.) for that parameter over ontogenetic growth was determined.

Results

Joint and limb kinematics

Although joint angles measured at mid-stance and relative stride length remained fairly similar, some kinematic parameters changed significantly during ontogeny. At a 0.40DF, hip, knee, ankle and TMP joint angles measured in a parasagittal plane (lateral view) during treadmill locomotion did not change significantly with growth (Fig. 2A). Mean joint angles at mid-stance for the hip (90±8°; regression slope ±95%CI: 0.13±0.24, R^2=0.07), knee (90±10°; 0.04±0.30, R^2=0.01), ankle (128±6°; 0.06±0.17, R^2=0.03) and TMP (111±4°; –0.03±0.12, R^2=0.01), were not significantly different from those measured at the times of peak bone strains (Fig. 2C). Similarly, stride length normalized to total leg length did not change significantly with growth (2.32±0.21 leg lengths, proportional to $M_b^{0.01\pm0.04}$, R^2=0.02) as both leg length and stride length scaled with isometry relative to M_b (leg length$\propto M_b^{0.35\pm0.04}$, R^2=0.94; stride length$\propto M_b^{0.36\pm0.05}$, R^2=0.88). In contrast, the duration of foot contact increased significantly with growth ($\propto M_b^{0.09\pm0.04}$, R^2=0.55), while stride frequency decreased ($\propto M_b^{-0.10\pm0.04}$, R^2=0.70).

Ontogenetic changes in peak limb loads

Peak resultant ground reaction forces ($\mathbf{F}_R$) normalized to body weight did not change significantly during ontogeny in relative magnitude, orientation, or timing. When running over ground at 0.40DF (0.42±0.02, N=25), peak $\mathbf{F}_R$=2.2±0.3BW, regardless of M_b (Fig. 2B, –0.004±0.006, R^2=0.08). Similarly, the orientation of peak $\mathbf{F}_R$ in both the fore–aft direction of travel and medial–lateral direction, relative to the vertical reference frame centered at the foot, did not change significantly with size. Peak $\mathbf{F}_R$ was oriented 1.7±5.1° posterior (regression slope *versus* M_b ±95%CI: 0.07±0.13, R^2=0.05, Fig. 2C) and 1.9±5.2° lateral (0.10±0.13, R^2=0.10) relative to the vertical. The relative timing of peak $\mathbf{F}_R$ at 0.40DF was also similar during ontogeny (–0.03±0.18, R^2=0.004), occurring at 34±7% of the way through stance.

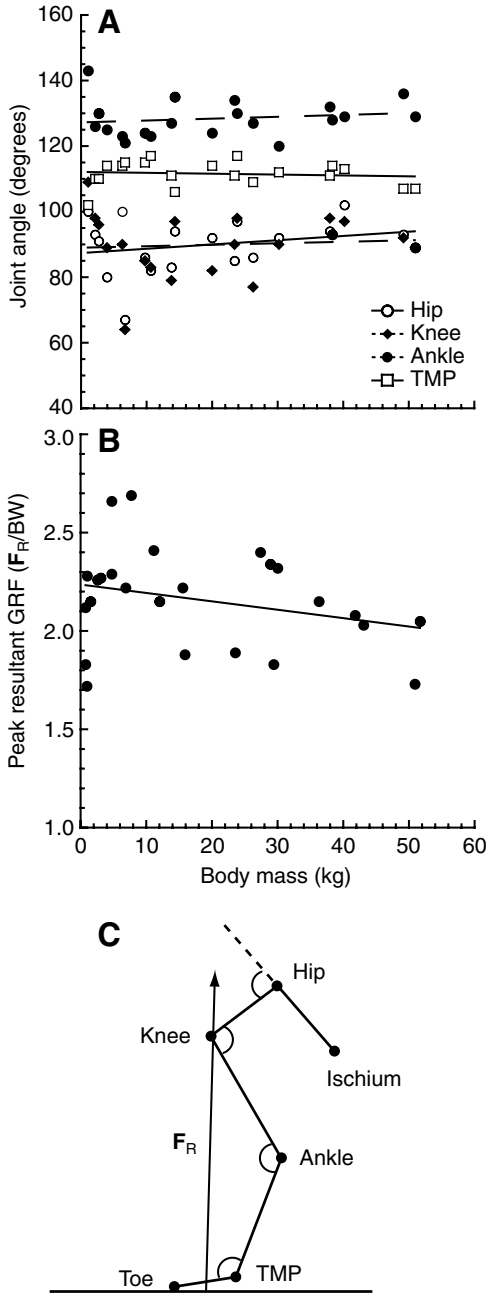

Fig. 2. (A) The mean joint angles at mid-stance *versus* body mass while running with a 0.40 duty factor (DF), for the hip (open circles), knee (closed diamonds), ankle (closed circles) and TMP joints (open squares). The equations for the least-squares regression lines (±95%CI for the slope) are as follows: hip, y=87.3+0.13x (±0.24, R^2=0.07); knee, y=88.9+0.04x (±0.30, R^2=0.01); ankle, y=127.2+0.06x (±0.17, R^2=0.03), and TMP, y=112.0–0.03x (±0.12, R^2=0.01). (B) Peak resultant ground reaction forces ($\mathbf{F}_R$) normalized by body weight when running with a 0.40DF; y=2.24–0.004x (±0.006, R^2=0.08). (C) A scaled stick figure representation of the typical emu hindlimb posture at the time of peak bone strains when running with a 0.40DF. The joint angles (mean ± s.d.) are as follows: hip, 86±9°; knee, 97±12°; ankle, 129±7°; TMP, 120±7°. $\mathbf{F}_R$ is oriented 1.7° from the vertical axis in the fore–aft plane, passing near the knee. Even though the TMP joint is inclined slightly relative to the toe (9°), the foot was flat on the ground at the time of peak bone strains.

Peak bone strain versus size in the femur and TBT

In vivo bone strains measured in the femur generally increased in magnitude with mass, but were oriented similarly through growth relative to the long axis of the bone. Principal tension and compression on the cranial femur surface (Fig. 3A) increased similarly and significantly in magnitude during ontogeny (Fig. 4A, Table 1, tension$\propto M_b^{0.24\pm0.16}$, R^2=0.50; compression$\propto M_b^{-0.29\pm0.17}$, R^2=0.55), as did the principal strains on the caudal surface (Fig. 4B, tension$\propto M_b^{0.39\pm0.28}$, R^2=0.48; compression$\propto M_b^{-0.36\pm0.28}$, R^2=0.43). The greatest axial strains measured with the single element gauge on the lateral femoral surface were generally tensile, and did not change significantly with size (Fig. 4C, tension$\propto M_b^{-0.06\pm0.47}$, R^2=0.003).

Though strains in the cranial and caudal cortices of the femur increased in magnitude, the orientation of the principal strains, relative to the bone's long axis, were very similar throughout growth. On the cranial surface of the left femur, peak principal tension and compression were consistently oriented at 37±4° (0.08±0.21, R^2=0.06) and –53±4° (0.08±0.20, R^2=0.06) relative to the bone's long axis, respectively, such that the principal tension was aligned in a proximal–medial to distal–lateral

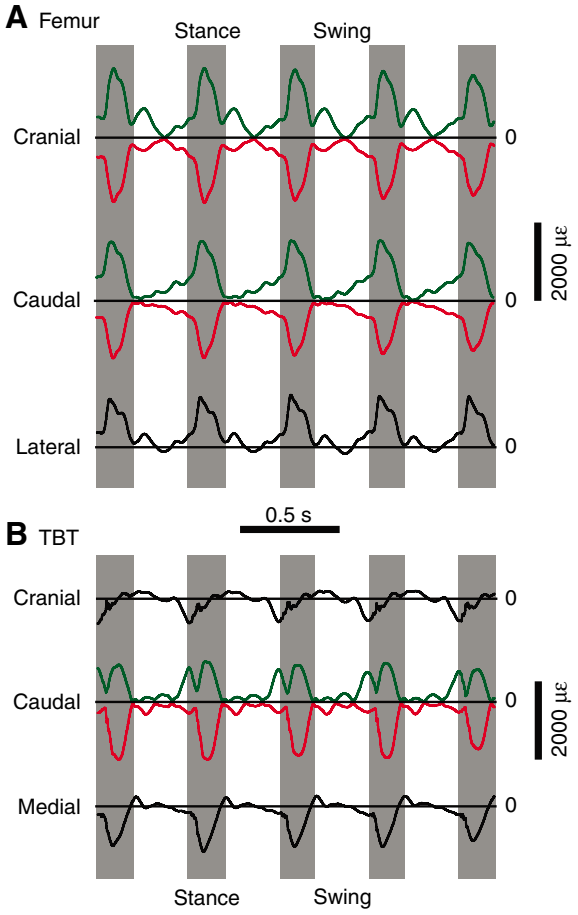

Fig. 3. Representative principal and axial bone strains for the (A) femur and (B) TBT for five footfalls from a 36 week old, 27 kg emu running with a 0.41DF at 5.40 m s^{-1}. Principal tensile strains, green; principal compressive strains, red. The axial strains measured from the lateral femur and cranial and medial TBT are in black. The shaded bars represent the stance phase during the locomotor cycle.

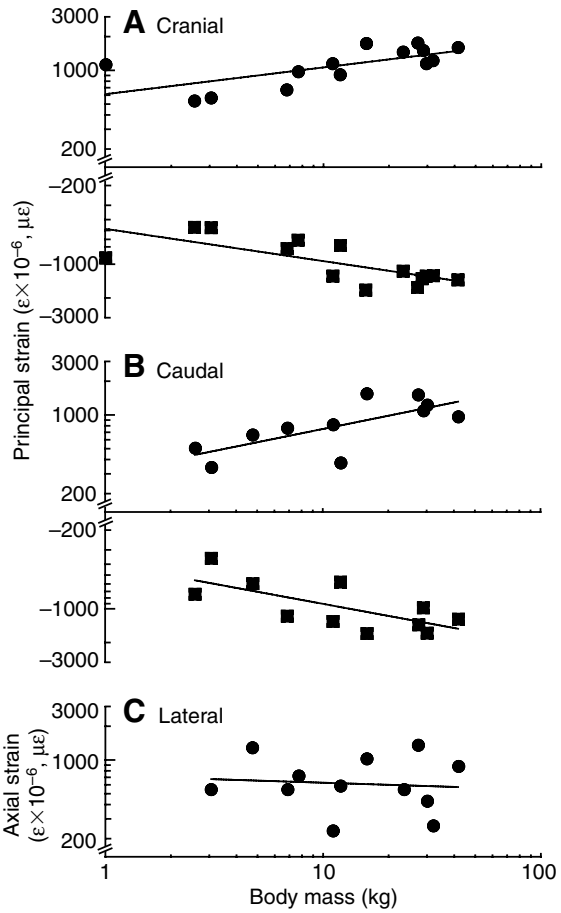

Fig. 4. Mean peak bone strains *versus* body mass for the emu femur on logarithmic axes. Mean peak principal tensile and compressive strains for the (A) cranial and (B) caudal surfaces and (C) mean peak tensile axial strains for the lateral surface of the emu femur as the birds ran at a 0.40DF. Tensile strains, circles; compressive strains, squares. In A, the equations for the least-squares regression lines for the peak principal tensile and compressive strains are $y=612x^{0.24\pm0.16}$ (R^2=0.50, N=14) and $y=-482x^{-0.29\pm0.17}$ (R^2=0.55), respectively. In B, for principal tension, $y=304x^{0.39\pm0.28}$ (R^2=0.48, N=11) and principal compression, $y=-399x^{-0.36\pm0.28}$ (R^2=0.43). In C, for axial tension, $y=721x^{-0.06\pm0.47}$ (R^2=0.003, N=12). In A and B, the slopes and 95%CIs of the power lines for the principal compressive strains were taken on the absolute values of these strains, but plotted in the figure on the negative compressive values for clarity. As multiple trials at this DF were not collected for all birds, error bars have been omitted for consistency.

direction relative to the long axis of the bone, with the principal compression oriented at 90° to the principal tension (Fig. 5A). On the caudal surface, the peak principal tension and compression were consistently aligned at 49±5° (0.14±0.26, R^2=0.14) and –41±5° (0.13±0.26, R^2=0.12) relative to the long axis of the femur, respectively, so that the principal tension was oriented proximal–lateral to distal–medial. The timing of peak strains on each surface also did not change significantly with growth (P>0.05 in all cases), occurring on the cranial, caudal and lateral surfaces at 35±4%, 34±4% and 27±12% through stance, respectively (Fig. 3A).

Bone strains measured in the TBT also generally increased through ontogeny, though not as consistently as in the femur. Although the peak axial tensile and compressive strains, resulting from a strain reversal on the cranial TBT during each loading cycle (Fig. 3), increased with growth, the increase was not significant for the peak tensile strains (Fig. 6A, Table 1, $\propto M_b^{0.21\pm0.28}$, R^2=0.11), but was marginally significant for the peak compressive strains ($\propto M_b^{-0.324\pm0.316}$, R^2=0.09). Both principal tensile and compressive strains increased significantly on the caudal surface of the TBT (Fig. 6B; tension$\propto M_b^{0.26\pm0.11}$, R^2=0.68; compression$\propto M_b^{-0.32\pm0.10}$, R^2=0.75). However, the distribution of the data collected for the caudal TBT is skewed slightly and data from two young birds, below 10 kg M_b, have a relatively strong effect upon the regression slopes plotted on logarithmic axes. Nevertheless, regressions on non-log-transformed data gave similar results. Although peak axial strains measured from the medial surface of the TBT increased slightly with size, the increase was not significant (Fig. 6C, tension$\propto M_b^{0.15\pm0.25}$, R^2=0.09; compression$\propto M_b^{-0.12\pm0.17}$, R^2=0.08).

As for the cranial and caudal surfaces of the femur, the orientation of the peak principal tensile and compressive strains on the caudal surface of the left TBT were consistent through growth. The principal tension was consistently aligned at –65±7° (0.11±0.31, R^2=0.05) relative to the bone's long axis (Fig. 5B) while the principal compression was oriented at 25±7° (0.11±0.32, R^2=0.05) relative to the long axis and acted in a proximal–lateral to distal–medial direction. Principal strains collected from the cranial and medial surfaces of the two 75 week-old emu were also aligned well off the long axis of the TBT. In these two birds, principal tension and compression on the cranial surface were oriented at 45° relative to the long axis, with principal tension acting in a proximal–lateral to distal–medial direction. The principal tensile and compressive strains on the medial surface were oriented at –53° and 37° relative to the long axis of the bone, respectively, with the principal tension oriented in a proximal–cranial to distal–caudal direction.

As in the femur, the relative timing of peak strains on the three bone surfaces did not change significantly with growth (P>0.05 in all cases, except the peak principal tension on the caudal surface, which occurred 16% of the stance phase later from the smallest to the largest birds; caudal tension=0.33±0.23, R^2=0.49). Strains on the cranial TBT were biphasic with peak axial compression occurring at 4±8% through stance and peak axial tension 61±22% through stance (Fig. 3B). On the caudal surface of the TBT, peak principal compression and tension generally occurred at similar times: 38±8% and 45±7% through stance, respectively. Finally, peak axial strains on the medial surface of the TBT were also biphasic, with peak axial compression and tension occurring at 30±7% and 97±4% of the way through stance, respectively (Fig. 3B).

Ontogenetic bone loading patterns in the emu femur and TBT

Bone loading patterns in the emu femur and TBT were dominated by shear strains during growth, but also experienced significant amounts of axial bending and compression (Fig. 7). Shear strains in the femur increased through growth, showing a two- to threefold increase between 2.7 kg and 14 kg M_b, which were subsequently maintained through ontogeny (Fig. 8A). Axial compression and bending strains measured in both the

Table 1. *Scaling relationships for the in vivo strain data from the emu femur and tibiotarsus during ontogeny*

Strain (με)	a	c	95%CI	CI range	R^2
(A) Femur					
Cranial					
Principal tension	612	**0.24**	0.16	0.08, 0.40	0.50
Principal compression	–482	**–0.29**	0.17	–0.46, –0.12	0.55
Caudal					
Principal tension	304	**0.39**	0.28	0.11, 0.67	0.48
Principal compression	–399	**–0.36**	0.28	–0.64, –0.08	0.43
Lateral					
Axial tension	721	–0.06	0.47	–0.53, 0.41	0
(B) Tibiotarsus					
Cranial					
Axial tension	179	0.21	0.28	–0.07, 0.49	0.11
Axial compression	–165	**–0.324**	0.316	–0.640, –0.008	0.09
Caudal					
Principal tension	400	**0.26**	0.11	0.15, 0.37	0.68
Principal compression	–500	**–0.32**	0.10	–0.42, –0.22	0.75
Medial					
Axial tension	144	0.15	0.25	–0.10, 0.40	0.09
Axial compression	–542	–0.12	0.17	–0.29, 0.05	0.08

a and c are values for the *y*-intercept and exponent, respectively, in the exponential equation $y=ax^c$, where x is body mass (M_b) and y is the dependent variable.

The 95% confidence interval (CI) and corresponding range represent the variation about the value for the scaling exponent (c).

Significant relationships are indicated in bold when the CI range does not overlap zero.

με, microstrain, $\varepsilon\times10^{-6}$.

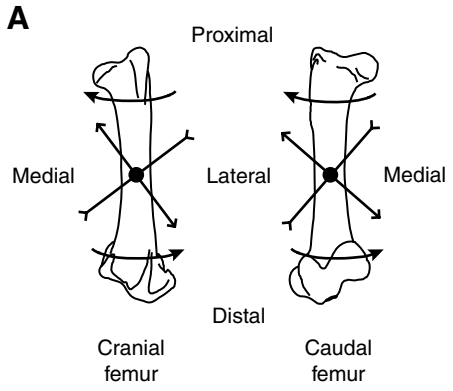

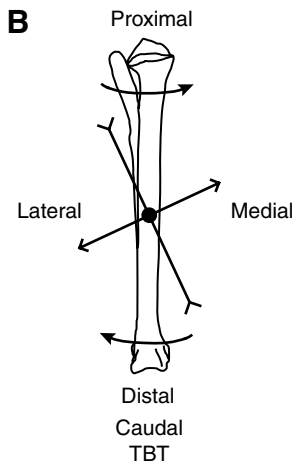

cranial–caudal (CC) and medial–lateral (ML, not shown) directions did not change significantly with growth up to 25 kg M_b (Fig. 8A, $P>0.05$ in all cases). However, given the high axial compression and bending strains measured for one bird over 25 kg M_b, an ontogenetic increase in bending and axial compression may occur at larger sizes.

Throughout growth, shear strains in the emu femur were generally dominant. Peak shear strains measured on the cranial and caudal surfaces of the femur were 3–4 times greater than the strains due to axial compression or CC bending, while peak CC bending strains were 1.6 times those due to axial compression. Data from the single bird larger than 25 kg suggested that at larger sizes, bending, axial compression, and

Fig. 5. Cranial view of the femur and caudal views of the femur and TBT of an adult emu, showing the mean principal strain orientations on the different bone surfaces and the corresponding direction of torsional loading. In the femur (A), the principal tension (black arrows) measured at the bone's mid-shaft is oriented at 37° and 49° relative to the long axis of the bone on the cranial and caudal surfaces, respectively. The principal compression (reverse black arrows) is oriented at 90° to the principal tension. The orientation of the strains in the femur indicate torsional loading of the bone, acting to rotate the proximal end medially about the long axis relative to the distal end (as viewed from the cranial surface, grey arrows). (B) In the TBT (shown with adjacent fibula), the principal compression is oriented at 25° relative to the long axis, indicating a significant torsional component acting to rotate the proximal end medially relative to the distal end (as viewed from the caudal surface, grey arrows). The lengths of the black arrows representing the principal strains are not scaled to the strain magnitudes measured on these bone surfaces.

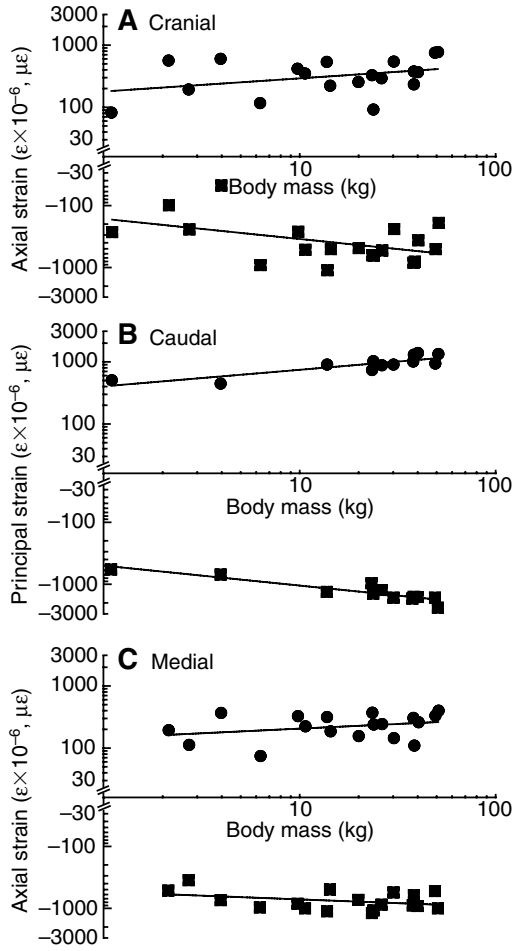

Fig. 6. Mean peak bone strains *versus* body mass for the emu TBT on logarithmic axes. Mean peak axial tensile and compressive strains for the (A) cranial and (C) medial surfaces and (B) mean peak principal tensile and compressive strains from the caudal surface of the emu TBT while the birds ran at a 0.40DF. Tensile strains, circles; compressive strains, squares. In A, the equations for the least-squares regression lines for the peak axial tensile and compressive strains are $y=179x^{0.21\pm0.28}$ (R^2=0.11, N=19) and $y=-165x^{-0.324\pm0.316}$ (R^2=0.09), respectively. In B, for principal tension, $y=400x^{0.26\pm0.11}$ (R^2=0.68, N=12) and principal compression, $y=-500x^{-0.32\pm0.10}$ (R^2=0.75). In C, for axial tension, $y=144x^{0.15\pm0.25}$ (R^2=0.09, N=18) and axial compression, $y=-542x^{-0.12\pm0.17}$ (R^2=0.08). The slopes and 95%CIs of the power lines for the compressive strains, were taken on the absolute values of these strains, but plotted in the figure on the negative compressive values for clarity. As multiple trials at this DF were not collected for all birds, error bars have been omitted for consistency.

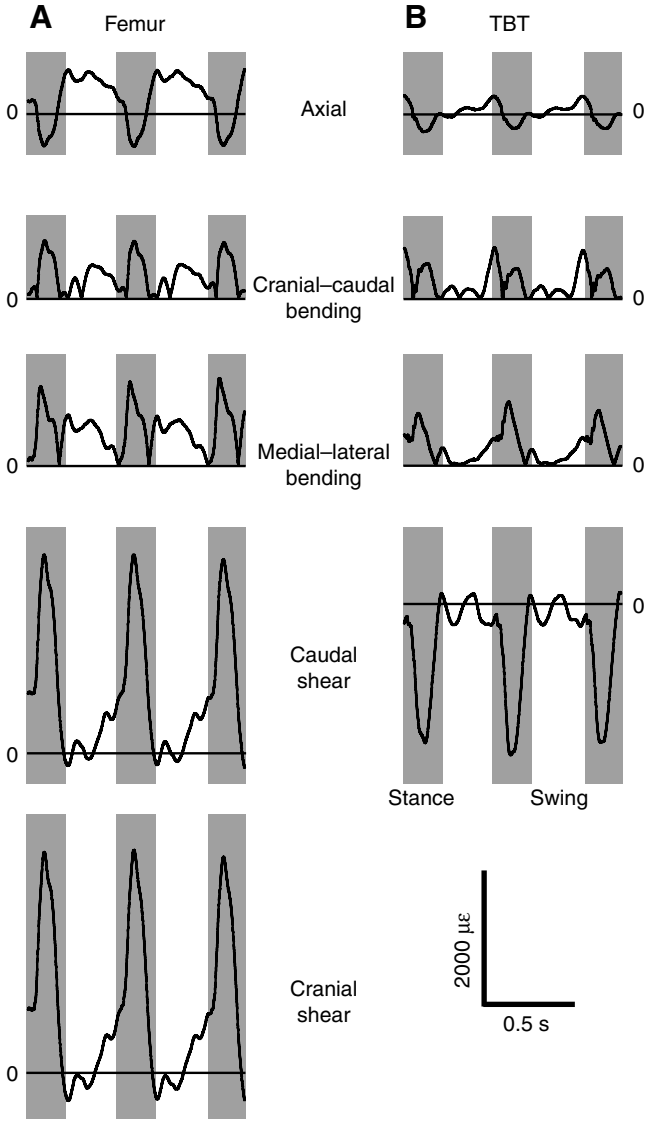

Fig. 7. Representative axial, cranial–caudal and medial–lateral axial bending, and caudal and cranial shear strains for (A) the femur and (B) TBT for three footfalls from a 36-week-old, 27 kg emu running with a 0.41DF at 5.40 m s^{-1}. The shaded bars represent the stance phase during the locomotor cycle. Note that the peak shear strains for the caudal surface of the TBT are negative while those for the femur are positive. This is consistent with the primary torques on these bones acting in opposite directions, where the proximal ends of the femur and TBT experienced medial and lateral torsion, respectively, when viewed from the cranial surfaces of the bones.

shear strains may contribute fairly equally to the mechanical loads transmitted within the femur.

In the emu TBT, significant increases in shear, axial bending, and compressive strains occurred with growth. However, as in the femur, shear strains consistently dominated at the caudal TBT mid-shaft (Fig. 7B). Axial compression and bending strains measured in the CC direction increased significantly during ontogeny (Fig. 8B; axial compression$\propto M_b^{-0.52\pm0.27}$, R^2=0.48; CC bending$\propto M_b^{0.38\pm0.30}$, R^2=0.38), although strains resulting from bending in the ML direction varied little with growth (ML bending$\propto M_b^{0.10\pm0.32}$, R^2=0.03, not shown). Shear strains measured on the caudal TBT also increased significantly during ontogeny (shear strain$\propto M_b^{-0.66\pm0.22}$, R^2=0.69), and exceeded the axial strains measured at this and the other sites. Peak shear strains on the caudal TBT were about 6.7 and 2.7 times the peak axial and cranial–caudal bending strains, respectively. Additionally, in the two 75-week-old birds, the relative amounts of strain due to bending, axial compression, and shear measured on the cranial and medial surfaces of the TBT were similar to the overall loading patterns observed on the caudal TBT throughout growth.

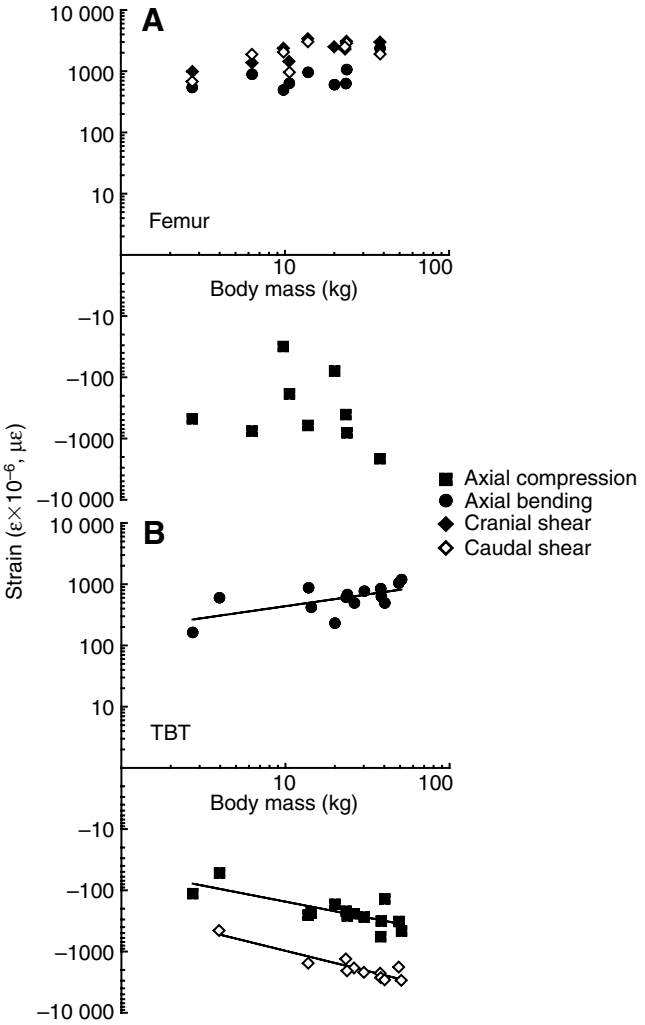

Fig. 8. Axial compression, cranial–caudal axial bending, and cranial and caudal shear strains *versus* body mass on logarithmic axes for (A) the femur and (B) TBT. Closed squares, axial compression; closed circles, cranial–caudal axial bending; closed diamonds, cranial shear strains; open diamonds, caudal shear strains. In A, given the non-linearity of the trends for the femur, even on logarithmic axes, regression equations were not calculated. In B, axial compression, $y=-46x^{-0.52\pm0.27}$ (R^2=0.48, N=14); cranial-caudal axial bending, $y=181x^{0.38\pm0.30}$ (R^2=0.38, N=14); caudal shear, $y=-212x^{-0.66\pm0.22}$ (R^2=0.69, N=11). In B, the slopes and 95%CIs of the power lines for the axial compressive and caudal shear strains were taken on the absolute values of these strains, but plotted in the figure on the negative values for clarity. As multiple trials at this DF were not collected for all birds, error bars have been omitted for consistency.

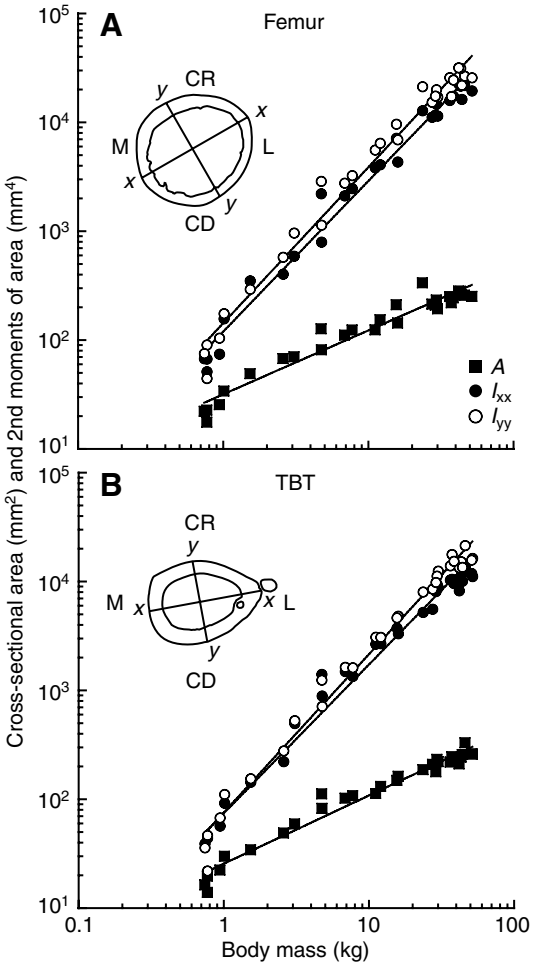

Fig. 9. Mid-shaft cross-sectional area (A) and the second moments of area across the x and y axes (I_{xx} and I_{yy}, respectively) for the emu (A) femur and (B) TBT *versus* body mass on logarithmic axes. Femur and TBT mid-shaft cross-sections from an adult bird (>8 years old, 37 kg) demonstrate the anatomical position of the axes about which the second moments of area were typically distributed, where I_{xx} (closed circles) and I_{yy} (open circles) are distributed about the x–x and y–y axes, respectively. (A) A: $y=32x^{0.59\pm0.06}$ (R^2=0.87); I_{xx}: $y=120x^{1.38\pm0.07}$ (R^2=0.95); I_{yy}: $y=143x^{1.43\pm0.08}$ (R^2=0.90). (B), A: $y=26x^{0.63\pm0.05}$ (R^2=0.95); I_{xx}: $y=74x^{1.37\pm0.08}$ (R^2=0.93); I_{yy}: $y=76x^{1.45\pm0.07}$ (R^2=0.92). The scaling patterns for the polar moments of area, J, were omitted for clarity as, being the sum of I_{xx} and I_{yy}, they nearly overlie the trends for I and scaled very similarly, J_{FEMUR}: $y=264x^{1.410\pm0.075}$ (R^2=0.93) and J_{TBT}: $y=150x^{1.41\pm0.07}$ (R^2=0.93).

Ontogenetic changes in bone geometry

Femoral mid-shaft cross-sectional geometry scaled variably through growth. Femoral cross-sectional area A scaled with negative allometry (Fig. 9A, Table 2, $A\propto M_b^{0.59\pm0.06}$, R^2=0.87), becoming relatively smaller as the birds increased in mass during ontogeny. The axes about which the minimum and maximum second moments of area were distributed in the femur did not correspond closely to the anatomical CC or ML axes (Fig. 9A). Instead, I_{yy}, which was generally the greater of the two measurements, was distributed about an axis oriented in a cranial–medial to caudal–lateral position, with I_{xx} at 90° to it. Both second moments of area scaled similarly with size, either with isometry (Fig. 9A, $I_{xx}\propto M_b^{1.38\pm0.07}$, R^2=0.95) or with slight positive allometry ($I_{yy}\propto M_b^{1.43\pm0.08}$, R^2=0.90). Throughout ontogeny, I_{xx} and I_{yy} were similar in magnitude, reflecting the fairly symmetrical circular shape of the femoral mid-shaft. Consequently, the polar moment of area ($J=I_{xx}+I_{yy}$) also scaled similarly with very slight positive allometry (not shown, $\propto M_b^{1.410\pm0.075}$, R^2=0.93).

The TBT mid-shaft cross-sectional geometry scaled similar to the femur, with the cross-sectional area scaling isometrically

Table 2. *Scaling relationships for the cross-sectional bone geometry, curvature, and percent ash content in the emu femur and tibiotarsus during ontogeny*

	a	c	95%CI	CI range	R^2
(A) Femur					
Cross-sectional geometry					
A (mm^2)	32	**0.59**	0.06	0.53, 0.65	0.87
I_{xx} (mm^4)	120	1.38	0.07	1.31, 1.45	0.95
I_{yy} (mm^4)	143	**1.43**	0.08	1.35, 1.51	0.90
J (mm^4)	264	**1.410**	0.075	1.335, 1.485	0.93
Curvature					
C_{CC}	0.77	**–0.20**	0.08	–0.28, –0.12	0.57
C_{ML}	0.82	**–0.12**	0.06	–0.18. –0.06	0.42
Ash content (%)	52	**0.070**	0.010	0.060, 0.080	0.88
(B) Tibiotarsus					
Cross-sectional geometry					
A (mm^2)	26	0.63	0.05	0.58, 0.68	0.95
I_{xx} (mm^4)	74	1.37	0.08	1.29, 1.45	0.93
I_{yy} (mm^4)	76	**1.45**	0.07	1.38, 1.52	0.92
J (mm^4)	150	**1.41**	0.07	1.34, 1.48	0.93
Curvature					
C_{CC}	0.71	**–0.19**	0.14	–0.33, –0.05	0.19
C_{ML}	0.82	**–0.15**	0.10	–0.25, –0.05	0.32
Ash content (%)	54	**0.055**	0.009	0.046, 0.064	0.83

a and c are values for the y-intercept and exponent, respectively, in the exponential equation $y=ax^c$, where x is body mass (M_b) and y is the dependent variable.

The 95% confidence interval (CI) and corresponding range represent the variation about the value for the scaling exponent (c).

Significant relationships are indicated in bold when the CI range does not overlap zero (bone curvature, percent ash content) or is significantly different from isometry (cross-sectional geometry; $A\alpha M_b^{0.67}$; I,$J\alpha M_b^{1.33}$).

(Fig. 9B, Table 2; $A\propto M_b^{0.63\pm0.05}$, R^2=0.95). For the TBT, the axes about which the second moments of area were distributed closely approximated the ML (x–x) and CC (y–y) axes (Fig. 9B). As for the femur, the second moments of area scaled with isometry ($I_{xx}\propto M_b^{1.37\pm0.08}$, R^2=0.93) or slight positive allometry ($I_{yy}\propto M_b^{1.45\pm0.07}$, R^2=0.92), reflecting a growth trajectory with slight relative expansion in the ML dimensions of the bone. Correspondingly, the polar moment of area scaled with slight positive allometry ($\propto M_b^{1.41\pm0.07}$, R^2=0.93). Similar magnitudes of I_{xx} and I_{yy} again reflected the generally circular shape of the TBT during ontogenetic growth.

Ontogenetic changes in bone curvature and mineral content

Significant changes in longitudinal bone curvature and percent mineral content of each bone were also observed during ontogenetic growth. The caudal and medial concave curvatures (C_{CC} and C_{ML}, respectively) of the emu femur and TBT decreased significantly with size (Fig. 10, Table 2, femur: $C_{CC}\propto M_b^{-0.20\pm0.08}$, R^2=0.57; $C_{ML}\propto M_b^{-0.12\pm0.06}$, R^2=0.42; TBT: $C_{CC}\propto M_b^{-0.19\pm0.14}$, R^2=0.19; $C_{ML}\propto M_b^{-0.15\pm0.10}$, R^2=0.32). Percent mineral content by mass increased significantly and similarly in each bone, ranging from 49% to 72% over the age range sampled. The slope of the trend for the femur (Fig. 11, Table 2, $\propto M_b^{0.070\pm0.010}$, R^2=0.88) was not significantly different from the ontogenetic slope for the TBT ($\propto M_b^{0.055\pm0.009}$, R^2=0.83).

Discussion

Ontogenetic increases in bone strain in the emu hindlimb

Although the distribution of mid-shaft strains within the emu femur and tibiotarsus (TBT) remained similar during ontogeny, bone strain magnitudes generally increased with age and growth in size. This increase largely appears to result from the ontogenetic scaling patterns of the cross-sectional geometry of these two bones while relative limb loads were maintained during growth. Indeed, the cross-sectional area of the femur scaled with negative allometry, and no other measurement of the cross-sectional geometry scaled with sufficient positive allometry to maintain functional strains at similar levels in either bone during ontogenetic growth. Only I_{yy}, in both the femur and TBT, matched expectations for elastic similarity [$A\propto M_b^{0.75}$, I and $J\propto M_b^{1.50}$, following McMahon (McMahon, 1975)], whereas other cross-sectional measures scaled close to isometry, which was well below scaling expectations for the maintenance of stress/strain similarity ($A\propto M_b^{1.0}$, I and $J\propto M_b^{1.67}$). Because normalized ground reaction forces (GRFs) exerted by the limb at 0.40DF remained fairly constant at 2.2BW and were oriented similarly relative to the limb throughout growth, the generally isometric growth of the limb skeleton resulted in increased strain magnitudes.

Reduced bone curvature and increased mineralization during growth likely mitigated the increase in locomotor bone strains engendered by the ontogenetic patterns in bone geometry and limb loading. Longitudinal curvature of the femur and TBT decreased significantly, producing relatively straighter bones in older, larger birds, serving to reduce bending strains caused by hip and ankle extensor muscle forces transmitted along the bones' lengths during stance (Biewener, 1983). The ontogenetic increase in ash content in both bones likely reflects an increase

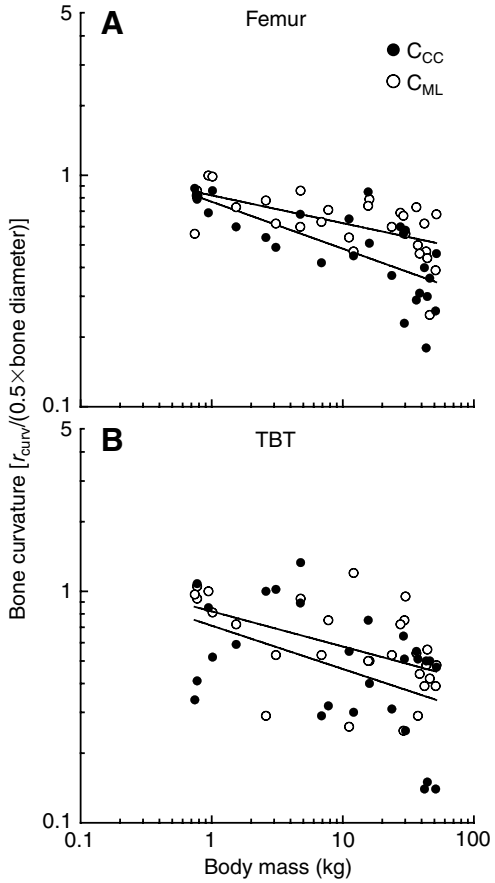

Fig. 10. Cranial–caudal (C_{CC}) and medial–lateral (C_{ML}) longitudinal bone curvature *versus* body mass on logarithmic axes for the emu (A) femur and (B) TBT. C_{CC}, closed circles; C_{ML}, open circles. In A, C_{CC}: $y=0.77x^{-0.20\pm0.08}$ (R^2=0.57); C_{ML}: $y=0.82x^{-0.12\pm0.06}$ (R^2=0.42). In B, C_{CC}: $y=0.71x^{-0.19\pm0.14}$ (R^2=0.19); C_{ML}: $y=0.82x^{-0.15\pm0.10}$ (R^2=0.32).

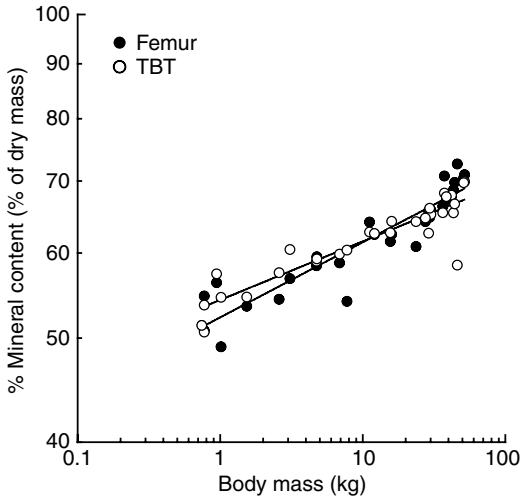

Fig. 11. Percent mineral content by mass *versus* body mass on logarithmic axes for the emu femur (closed circles) and TBT (open circles). Femur: $y=52x^{0.070\pm0.010}$ (R^2=0.88); TBT: $y=54x^{0.055\pm0.009}$ (R^2=0.83).

in bone mineralization and thus, the bones' elastic moduli (Currey and Pond, 1989; Brear et al., 1990), helping to decrease peak strains in older bone tissue. The mitigation of locomotor bone strains in the femur and TBT by increased mineralization and reduced curvature resulted in peak bone strains that increased only twofold from 3 weeks to >8 years of age, despite a 46-fold increase in body mass.

Although bone strains increased significantly at certain mid-shaft sites, axial strains on the lateral femur and medial TBT remained fairly constant through growth. However, this may reflect the limitation of using single element gauges on these surfaces, which would not have measured the ontogenetic increase in shear strains observed using rosette strain gauges on the cranial and caudal surfaces of the bones.

Torsion versus axial loading in tetrapod hindlimb bones

Shear strains induced by torsion dominated the loading environment measured at most mid-shaft sites of the emu femur and TBT throughout the majority of ontogenetic growth. The orientation of the principal strains in the femur indicated torsion acting to rotate the proximal end of the bone medially (when viewed from the cranial aspect, Fig. 5A) relative to its fixed distal end at the knee. Principal strains measured on the caudal surface of the emu TBT during ontogeny, and from the three surfaces of the two 75-week-old birds, reflected significant torsion in the TBT as well, acting to rotate the proximal end medially relative to a fixed ankle (as viewed from the caudal surface of the bone, Fig. 5B). These loading patterns indicate that ontogenetic scaling of J (and likely bone shear modulus) is most critical to resisting functional strains during growth. Although shear modulus was not measured, J failed to scale with sufficient positive allometry to maintain shear strains at similar levels through growth.

Studies of only two avian taxa to date suggest that torsion may be the dominant loading mode in the long bones of the avian hindlimb. Throughout ontogenetic growth, peak principal strains measured in the emu femur and TBT were consistently oriented at least 37° and 25° off the long axis of the bones, respectively. A similar pattern and orientation of torsional loading in the chicken femur has also been observed (Carrano and Biewener, 1999). In the chicken TBT, principal strains were oriented 25–44° from the bone's long axis (Biewener et al., 1986; Biewener and Bertram, 1993), similar in range and orientation to the principal strains measured in the emu TBT. Although the relative contributions of the bending, axial and shear strains were not calculated for the chicken TBT, peak shear strains in the chicken femur were more than ten times peak axial compressive strains and more than twice the bending strains (Carrano and Biewener, 1999). By comparison, peak shear strains in the emu femur were 3–4 times greater than the bending and axial strains. Thus, differences in femoral loading between the two taxa are characterized most by differences in the relative amounts of bending *versus* axial strain, not shear strain.

The differences in the relative amounts of bending and axial compression in the femora of these two taxa largely result from interspecific scaling patterns for the avian femur. Although a more upright posture has been argued to decrease musculoskeletal loading in larger mammals and birds (Biewener, 1989; Gatesy and Biewener, 1991), the emu femur

was found to be oriented ~37° below the horizontal when peak strains occurred, compared with a femoral orientation ~45° below the horizontal in chickens. Thus, a vertically oriented reaction force would be expected to produce a relatively larger bending moment in the emu femur than in chickens, if femoral length scaled isometrically. However, bird femora typically become shorter relative to their diameters across size [length$\propto$diameter$^{0.68–0.86}$ (Gatesy, 1991b; Olmos et al., 1996)], and both the cross-sectional area and second moments of area scale with strong positive allometry in birds [$A\propto M_b^{0.84}$, $I_{MAX}\propto M_b^{1.69}$ (Cubo and Casinos, 1997; Cubo and Casinos, 1998)]. Considered together, these factors indicate an effective increase in the bending resistance of emu femora relative to the femora of much smaller chickens, consistent with relatively less bending in emu femora, despite being held closer to the horizontal plane.

Birds are not the only tetrapods whose hindlimb bones experience primarily torsional loading during terrestrial locomotion. Significant shear strains have also been recorded from the femora of alligators and iguanas, as well as the alligator tibia (Blob and Biewener, 1999). Principal strains in the femora of these animals were oriented in a similar direction as in the bird femur (>29° from the bone's long axis), indicating medial rotation of the proximal end of the bone, relative to a fixed knee. Similarly, the alligator tibia also experiences substantial torsion that is directionally consistent with the torsion observed in the avian TBT.

Although rotation about the long axes of the limb elements of 'sprawling' tetrapods has long been recognized (Romer, 1922; Brinkman, 1980; Jenkins and Goslow, 1983; Gatesy, 1991a), it has not previously been clearly established for the hindlimb bones of terrestrial birds, other than for the study of chicken femoral strain patterns (Carrano and Biewener, 1999). Instead, avian hindlimb bones have often been assumed to be loaded primarily in longitudinal bending, consistent with the parasagittal orientation of the lower limb (Alexander et al., 1979b; Biewener, 1982; Cubo and Casinos, 1998; de Margerie et al., 2005). However, as noted above, the results here show that the emu femur and TBT are predominantly loaded in torsion. Torsional loading may be generally prevalent in the avian limb skeleton, as significant torsional shear strains were calculated for the chicken TMT (Judex et al., 1997) and have also been measured in the ulna and humerus during wing flapping (Rubin and Lanyon, 1985) and flight (Biewener and Dial, 1995). Indeed, the dominance of torsional loading associated with locomotor support and movement may well be common to most saurians (the phylogenetic group including birds, alligators and iguanas) (Gauthier, 1988) or, as noted previously (Blob and Biewener, 1999), it may be a common mode of skeletal loading among a diverse range of tetrapod groups (particularly non-cursorial ones) that have yet to be fully explored or recognized.

Relationships between ontogenetic strain patterns and limb bone scaling

Previous studies examining bone strain patterns during ontogeny have found that the orientation and distribution of strains within the limb bones typically remain fairly consistent throughout growth. However, strain magnitudes have been found to increase to varying extent with age and size. In the goat radius, mid-shaft strains increased significantly during ontogeny on all surfaces measured (Main and Biewener, 2004). For the emu examined here, principal strain magnitudes increased on the majority of mid-shaft surfaces examined, but generally remained uniform on the bone surfaces for which only axial strains were measured. In contrast, mid-shaft as well as proximal and distal bone strains in the growing chicken TBT remained fairly constant during ontogeny (Biewener et al., 1986). The absence of an increase in strain in the chicken TBT cannot be reconciled by the generally negative ontogenetic allometry of the bone's cross-sectional geometry (Biewener and Bertram, 1994). Consequently, although similar ontogenetic trends in strain magnitude were expected for the emu and chicken TBT, other factors, such as reduced limb loading and bone curvature or increased mineralization, would be required for the chicken TBT to explain the differences compared with the ontogenetic strain patterns for the emu.

Based on our study of the goat radius, we argued that negative allometry of bone cross-sectional geometry, especially for I_{CC} (I_{xx}), predisposed the radius to more predictable CC bending during ontogeny (Main and Biewener, 2004). Although the plane of bending rotated throughout stance, the bone's eccentric cross-sectional shape ($I_{yy}/I_{xx}>2$), which increased with size, was interpreted as likely contributing to the consistent ontogenetic loading patterns observed. In the emu femur and TBT, similar loading patterns were measured throughout ontogeny, even though these bones are more closely circular in shape. Thus, circular bone shape does not preclude consistent loading patterns through growth.

A circular cross-sectional shape is consistent with the predominance of shear that arises from torsional loading of these two bones during growth. Given a fixed amount of material, circular beam shapes provide the greatest resistance to torsional moments by maximizing J (Wainwright et al., 1976). Although the ratio of I_{yy} to I_{xx} changed significantly during ontogeny in the TBT (though not in the femur), it never exceeded 1.7 for either bone. Thus, the cross-sectional shapes of these bones may have resulted from stronger selection to enable resistance to torsional *versus* bending or axial loads, especially given the lower shear strength of bone compared with its strength in bending or axial tension and compression (Martin et al., 1998; Currey, 2002).

By maintaining a nearly circular shape and decreasing bone curvature through ontogeny, however, the bones of older emu may be more susceptible to less predictable bending directions (Bertram and Biewener, 1988), potentially increasing their fracture risk due to an aberrant limb loading circumstance or misstep. However, by being deeply invested in surrounding musculature, it is likely that the predominant forces experienced by both bones are muscular in origin and are constrained by anatomy to act in generally similar and predictable directions. The ontogenetic decrease in relative longitudinal curvature in both the femur and TBT might, however, indicate the importance of more predictable bending loads in younger birds that have relatively smaller limb muscle mass (total hindlimb muscle mass$\propto M_b^{1.19}$ for total hindlimb muscle mass) but experience external forces of similar relative magnitudes as adults. In the absence of a more eccentric cross-sectional bone

geometry and relatively less muscle mass, a more curved bone would pre-dispose bending and resulting strain distributions to a particular axis. This could be especially important to young, uncoordinated birds that face relatively larger environmental obstacles, which would pose less of a problem for adults that are more than 4.4 times their height.

In contrast to the negative growth allometry of jack rabbit metatarsals and goat radii (Carrier, 1983; Main and Biewener, 2004), which, in part, allows younger individuals of these taxa to perform similarly in absolute terms to adults without sacrificing safety against skeletal damage, the isometric or slight positive allometry of bone growth in emu suggests that selection for high levels of performance may not be as strong in young emu (Main and Biewener, 2006). These different pressures may also be reflected in the ontogenetic patterns of bone mineralization in these taxa. Over the ontogenetic ranges examined the percent ash content for the goat radius increased by ~4% of dry mass, compared with ~20% ontogenetic increase in the emu femur and TBT. This suggests that, compared with the adults, the radii of young goats have a relatively more robust morphology and are more similarly mineralized, whereas the femora and TBTs of adult emu retain their geometric proportions more similarly during growth but become substantially more mineralized. Consistent with these observations, bone strains increased 2.8-fold in the goat radius over a 6.3-fold ontogenetic increase in body mass, while the growing emu femur and TBT averaged only a twofold increase in peak bone strains across bone sites over a 46-fold increase in body mass.

The relationships between skeletal development and limb loading patterns described here remain tentative, emphasizing the need for additional work to examine skeletal ontogeny and the biomechanics of limb loading in a wider range of animals operating under a variety of locomotor activities. Such studies can help to test functional hypotheses related to emerging patterns of skeletal form and function during ontogenetic growth. Ultimately, these studies will facilitate a better understanding of why tetrapod limb bones have evolved the vast variety of shapes and sizes that exist and how various selective pressures relate to the locomotor ecology of diverse vertebrate taxa. To achieve such an understanding will require a broadly integrative and comparative approach to skeletal mechanics and development that combines studies of limb loading, *in vivo* bone strain, and skeletal morphology, as was carried out here in our study of emu limb bone growth and mechanics.

List of abbreviations and symbols

ϕ	angle of a principal strain relative to the bone's long axis
$\mu\varepsilon$	microstrain, strain$\times10^{-6}$
A	cross-sectional area
BW	body weight (in N)
CC	cranial–caudal
C_{CC}, C_{ML}	cranial–caudal, medial–lateral longitudinal bone curvatures
CI	confidence interval
DF	duty factor
$\mathbf{F}_R$	resultant ground reaction force
GRF	ground reaction force
I	second moment of area
J	polar moment of area
M_b	body mass
ML	medial–lateral
TBT	tibiotarsus
TMP	tarsometatarsal–phalangeal joint
TMT	tarsometatarsus

This work would not have been possible without the assistance of many of the members of the Concord Field Station. We would especially like to thank Pedro Ramirez for his excellent care of the emu and Craig McGowan, Polly McGuigan, Rebecca Mitchell, Jim Usherwood, and Ty Hedrick who were particularly giving of their time during surgeries, data collection and dissections. We would also like to thank Dan Lieberman for the NIH Image cross-sectional geometry macro and Stan Johnson of Songline Emu Farm for advice concerning the care and rearing of young emu. This manuscript was improved by the helpful comments of two anonymous reviewers. This work was supported in part by the Chapman Fund (Harvard University).

References

Alexander, R. McN. and Jayes, A. S. (1983). A dynamic similarity hypothesis for gaits of quadrupedal mammals. *J. Zool. Lond.* **201**, 135-152.

Alexander, R. McN., Jayes, A., Maloiy, G. and Wathuta, E. (1979a). Allometry of the limb bones of mammals from shrews (*Sorex*) to elephant (*Loxodonta*). *J. Zool. Lond.* **189**, 305-314.

Alexander, R. McN., Maloiy, G., Njau, R. and Jayes, A. (1979b). Mechanics of running of the ostrich (*Struthio camelus*). *J. Zool. Lond.* **187**, 169-178.

Bertram, J. E. A. and Biewener, A. A. (1988). Bone curvature: sacrificing bone strength for load predictability? *J. Theor. Biol.* **131**, 75-92.

Bertram, J. E. A. and Biewener, A. A. (1992). Allometry and curvature in the long bones of quadrupedal mammals. *J. Zool. Lond.* **226**, 455-467.

Biewener, A. A. (1982). Bone strength in small mammals and bipedal birds: do safety factors change with body size? *J. Exp. Biol.* **98**, 289-301.

Biewener, A. A. (1983). Allometry of quadrupedal locomotion: the scaling of duty factor, bone curvature and limb orientation to body size. *J. Exp. Biol.* **105**, 147-171.

Biewener, A. A. (1989). Scaling body support in mammals: limb posture and muscle mechanics. *Science* **245**, 45-48.

Biewener, A. A. (ed.) (1992). *In vivo* measurement of bone strain and tendon force. In *Biomechanics – Structures and Systems*, pp. 123-147. New York: Oxford University Press.

Biewener, A. A. (2005). Biomechanical consequences of scaling. *J. Exp. Biol.* **208**, 1665-1676.

Biewener, A. A. and Bertram, J. E. A. (1993). Skeletal strain patterns in relation to exercise training during growth. *J. Exp. Biol.* **185**, 51-69.

Biewener, A. A. and Bertram, J. E. A. (1994). Structural response of growing bone to exercise and disuse. *J. Appl. Physiol.* **76**, 946-955.

Biewener, A. A. and Dial, K. P. (1995). *In vivo* strain in the humerus of pigeons (*Columba livia*) during flight. *J. Morphol.* **225**, 61-75.

Biewener, A. A., Swartz, S. M. and Bertram, J. E. A. (1986). Bone modeling during growth: dynamic strain equilibrium in the chick tibiotarsus. *Calcif. Tissue Int.* **39**, 390-395.

Blob, R. W. and Biewener, A. A. (1999). *In vivo* locomotor strain in the hindlimb bones of *Alligator mississippiensis* and *Iguana iguana*: implications for the evolution of limb bone safety factor and non-sprawling limb posture. *J. Exp. Biol.* **202**, 1023-1046.

Brear, K., Currey, J. D. and Pond, C. M. (1990). Ontogenetic changes in the mechanical properties of the femur of the polar bear *Ursus maritimus*. *J. Zool. Lond.* **222**, 49-58.

Brinkman, D. (1980). The hindlimb step cycle of *Caiman sclerops* and the mechanics of the crocodile tarsus and metatarsus. *Can. J. Zool.* **58**, 2187-2200.

Carrano, M. T. and Biewener, A. A. (1999). Experimental alteration of limb posture in the chicken (*Gallus gallus*) and its bearing on the use of birds as analogs for dinosaur locomotion. *J. Morphol.* **240**, 237-249.

Carrier, D. (1983). Postnatal ontogeny of the musculo-skeletal system in the black-tailed jack rabbit (*Lepus californicus*). *J. Zool. Lond.* **201**, 27-55.

Carrier, D. and Leon, L. (1990). Skeletal growth in the California gull (*Larus californicus*). *J. Zool. Lond.* **222**, 375-389.
Cubo, J. and Casinos, A. (1997). Flightlessness and long bone allometry in Paleognathiformes and Sphenisciformes. *Neth. J. Zool.* **47**, 209-226.
Cubo, J. and Casinos, A. (1998). The variation of cross-sectional shape in the long bones of birds and mammals. *Ann. Sci. Nat. Zool.* **19**, 51-62.
Currey, J. D. (2002). *Bones: Structures and Mechanics*. Princeton: Princeton University Press.
Currey, J. D. and Pond, C. M. (1989). Mechanical properties of very young bone in the axis deer (*Axis axis*) and humans. *J. Zool. Lond.* **218**, 59-67.
Davies, S. J. J. F. (2002). *Ratites and Tinamous*. New York: Oxford University Press.
de Margerie, E., Sanchez, S., Cubo, J. and Castanet, J. (2005). Torsional resistance as a principal component of the structural design of long bones: comparative multivariate evidence in birds. *Anat. Rec. A* **282**, 49-66.
Full, R. J. and Tu, M. S. (1991). Mechanics of a rapid running insect: two-, four-, and six-legged locomotion. *J. Exp. Biol.* **156**, 215-231.
Gatesy, S. M. (1991a). Hindlimb movements of the American alligator (*Alligator mississippiensis*) and postural grades. *J. Zool. Lond.* **224**, 577-588.
Gatesy, S. M. (1991b). Hindlimb scaling in birds and other theropods: implications for terrestrial locomotion. *J. Morphol.* **209**, 83-96.
Gatesy, S. M. and Biewener, A. A. (1991). Bipedal locomotion: effects of speed, size and limb posture in birds and humans. *J. Zool. Lond.* **224**, 127-147.
Gauthier, J., Kluge, A. G. and Rowe, T. (1988). The early evolution of the Amniota. In *The Phylogeny and Classification of the Tetrapods*. Vol. 1 (ed. M. J. Benton), pp. 103-155. Oxford: Clarendon Press.
Herrel, A. and O'Reilly, J. C. (2006). Ontogenetic scaling of bite force in lizards and turtles. *Physiol. Biochem. Zool.* **79**, 31-42.
Herring, S. W., Pedersen, S. C. and Huang, X. (2005). Ontogeny of bone strain: the zygomatic arch in pigs. *J. Exp. Biol.* **208**, 4509-4521.
Jenkins, F. A., Jr and Goslow, G. E., Jr (1983). The functional anatomy of the shoulder of the Savannah Monitor lizard (*Varanus exanthematicus*). *J. Morphol.* **175**, 195-216.
Judex, S., Gross, T. S. and Zernicke, R. F. (1997). Strain gradients correlate with sites of exercise-induced bone-forming surfaces in the adult skeleton. *J. Bone Miner. Res.* **12**, 1737-1745.
Main, R. P. and Biewener, A. A. (2004). Ontogenetic patterns of limb loading, *in vivo* bone strains and growth in the goat radius. *J. Exp. Biol.* **207**, 2577-2588.
Main, R. P. and Biewener, A. A. (2006). In vivo bone strain and ontogenetic growth patterns in relation to life-history strategies and performance in two vertebrate taxa: goats and emu. *Physiol. Biochem. Zool.* **79**, 57-72.
Martin, R. B., Burr, D. B. and Sharkey, N. A. (1998). *Skeletal Tissue Mechanics*. New York: Springer-Verlag.
McMahon, T. A. (1975). Using body size to understand the structural design of animals: quadrupedal locomotion. *J. Appl. Physiol.* **39**, 619-627.
Olmos, M., Casinos, A. and Cubo, J. (1996). Limb allometry in birds. *Ann. Sci. Nat. Zool.* **17**, 39-49.
Patak, A. E. and Baldwin, J. (1998). Pelvic limb musculature in the emu *Dromaius novaehollandiae* (Aves: Struthioniformes: Dromaiidae): adaptations to high-speed running. *J. Morphol.* **238**, 23-37.
Pollock, C. M. and Shadwick, R. E. (1994). Allometry of muscle, tendon, and elastic energy storage capacity in mammals. *Am. J. Physiol.* **266**, R1022-R1031.
Richard, B. A. and Wainwright, P. C. (1995). Scaling the feeding mechanism of largemouth bass (*Micropterus salmoides*): kinematics of prey capture. *J. Exp. Biol.* **198**, 419-433.
Romer, A. S. (1922). The locomotor apparatus of certain primitive and mammal-like reptiles. *Bull. Am. Mus. Nat. Hist.* **46**, 517-606.
Rubenson, J., Heliams, D. B., Lloyd, D. G. and Fournier, P. A. (2004). Gait selection in the ostrich: mechanical and metabolic characteristics of walking and running with and without an aerial phase. *Proc. R. Soc. Lond. B Biol. Sci.* **271**, 1091-1099.
Rubin, C. T. and Lanyon, L. E. (1985). Regulation of bone mass by mechanical strain magnitude. *Calcif. Tissue Int.* **37**, 411-417.
Schmidt-Nielsen, K. (1997). *Animal Physiology: Adaptation and Environment*. Cambridge: Cambridge University Press.
Taylor, C. R., Schmidt-Nielsen, K. and Raab, J. L. (1970). Scaling of energetic cost of running to body size in mammals. *Am. J. Physiol.* **219**, 1104-1107.
Wainwright, S. A., Biggs, W. D., Currey, J. D. and Gosline, J. M. (1976). *Mechanical Design in Organisms*. Princeton: Princeton University Press.
Young, J. W. (2005). Ontogeny of muscle mechanical advantage in capuchin monkeys (*Cebus albifrons* and *Cebus paella*). *J. Zool. Lond.* **267**, 351-362.